

Full length article

Atomistic modeling of dislocation cross-slip in nickel using free-end nudged elastic band method

Dengke Chen ^a, Luke L. Costello ^a, Clint B. Geller ^b, Ting Zhu ^{a,c,*}, David L. McDowell ^{a,c,**}^a Woodruff School of Mechanical Engineering, Georgia Institute of Technology, Atlanta, GA, 30332, USA^b Naval Nuclear Laboratory, Bechtel Marine Propulsion Corporation, Pittsburgh, PA 15122, USA^c School of Materials Science and Engineering, Georgia Institute of Technology, Atlanta, GA 30332, USA

ARTICLE INFO

Article history:

Received 17 November 2018

Received in revised form

11 February 2019

Accepted 21 February 2019

Available online 25 February 2019

Keywords:

Dislocation

Cross-slip

Atomistic modeling

Activation energy

Free-end nudged elastic band method

ABSTRACT

Cross-slip of screw dislocations plays an important role in the plastic deformation of face-centered cubic (FCC) metals and alloys. Here we use the free-end nudged elastic band (FENEb) method to determine the atomistic reaction pathways and energy barriers of cross-slip in an FCC single crystal of Ni. We focus on the cross-slip process mediated by an array of pinning vacancy clusters in the form of stacking fault tetrahedra. We also study a competing process of screw glide by direct cutting of those pinning obstacles on the original slip plane. The activation energies of both cross-slip and obstacle-cutting are determined for different stresses, obstacle spacings and sizes. Using FENEb-calculated energy barriers, we construct dislocation mechanism maps to reveal the effects of resolved shear stress, obstacle spacing and size on the rate-controlling dislocation process for plastic deformation. We further evaluate the activation volumes of cross-slip and obstacle-cutting. The latter result emphasizes the notion of finite strength of the atomically sized pinning obstacles to dislocation motion and also validates the Nabarro scaling law of the linear dependence of activation volume on obstacle spacing.

© 2019 Acta Materialia Inc. Published by Elsevier Ltd. All rights reserved.

1. Introduction

Cross-slip occurs when a screw dislocation moves from one slip plane to another. This elementary plastic deformation mechanism plays an important role in the mechanical behavior of metals and alloys [1]. For example, cross-slip and double cross-slip provide a mechanism of dislocation multiplication that contributes to strain hardening [2]. Cross-slip is also considered as a relaxation mechanism associated with dynamic recovery in the stage III stress-strain diagram of FCC crystals [3]. Moreover, cross-slip can facilitate the formation of persistent slip bands during fatigue deformation of FCC crystals [4].

The mechanistic process of cross-slip has been the subject of active research for several decades [5–14]. In the classical Friedel-Escaig model of cross-slip in FCC crystals, the leading and trailing

partials of a dissociated screw dislocation locally constrict to form a perfect dislocation on the original slip plane, and then the constricted portion redissociates into a pair of leading and trailing partials on the cross-slip plane. As the two end points of the constricted portion move away from each other along the dislocation line, the entire screw dislocation transfers onto the cross-slip plane. While the Friedel-Escaig model captures the key features of cross-slip in FCC crystals, it remains a challenge to quantitatively predict the effects of driving stress, temperature, obstacle strength and geometry (e.g., size and spacing) on cross-slip. In early studies, researchers determined the critical stress and activation energy of cross-slip without considering the atomic processes in the dissociated dislocation core [7–13]. Hence various approximations were invoked and thus conferred substantial uncertainty to the predicted results.

In the past two decades, atomistic simulations have been performed to study screw dislocation cross-slip [15–27]. Among various atomistic modeling approaches, molecular dynamics (MD) simulations are limited to very short timescales and overdriven conditions, and first principles density functional theory calculations can only deal with extremely small systems. In contrast, atomistic reaction pathway modeling, which usually involves a

* Corresponding author. Woodruff School of Mechanical Engineering, Georgia Institute of Technology, Atlanta, GA, 30332, USA.

** Corresponding author. Woodruff School of Mechanical Engineering, Georgia Institute of Technology, Atlanta, GA, 30332, USA.

E-mail addresses: ting.zhu@me.gatech.edu (T. Zhu), david.mcdowell@me.gatech.edu (D.L. McDowell).

combined use of an empirical interatomic potential and the Nudged Elastic Band (NEB) method [28,29], enables the study of cross-slip in sufficiently large and realistic systems, while providing the atomic-level physical fidelity at the dislocation core. In particular, this approach allows quantitative prediction of the minimum energy path (MEP) [28,29] and thus the activation energy for a three-dimensional cross-slip process of a dislocation line. In the framework of transition state theory [30], the atomistically calculated activation energies and associated activation volumes can be compared with experimental measurements at the loading rates relevant to laboratory experiments [31,32], provided these unit processes are the rate-controlling dislocation mechanisms.

There are several important issues associated with the use of the NEB method for studying cross-slip in pure FCC metals such as Ni, Cu, Al, etc. First, the intrinsic lattice resistance to dislocation glide is negligibly small in most interatomic potential models of FCC metals. However, the NEB calculation of the energy barrier for cross-slip requires that the initial state on a MEP is a local energy minimum and thus serves as a reference state of zero energy [28,29]. This requirement raises the question of how a screw dislocation would be trapped at a local energy minimum in the absence of intrinsic lattice resistance. In fact, FCC metals inevitably contain various types of atomically-sized pinning obstacles to dislocation glide, such as individual point defects (vacancies and self-interstitials), clusters of these point defects, jogs on a dislocation line, as well as junctions of forest dislocations threading through the slip plane. These defects can serve as obstacles with finite pinning resistances for trapping a screw dislocation. For example, Rao et al. [22] have used the NEB method to study the cross-slip of a screw dislocation hindered by forest dislocations in FCC Ni and Cu. However, the atomistic process revealed in their work does not involve a typical relaxation response of dislocation breakaway from pinning obstacles that one would expect for cross-slip; moreover they have not studied the effects of stress and obstacle geometry on the energy barrier for cross-slip. In the present work, we study the cross-slip of a screw dislocation obstructed by an array of vacancy clusters. These clusters are taken as a representative type of atomically-sized obstacles that effectively trap the screw dislocation at a local energy minimum. The calculated MEP reveals the relaxation response of dislocation breakaway from pinning obstacles by cross-slip. The activation energies of cross-slip are determined for different applied stresses, obstacle spacings and sizes. It is noteworthy that in several previous studies of cross-slip in FCC metals [16,17,25,33], a special setup was used, in which the primary slip plane of the simulated screw dislocation was parallel to one side face of the simulation supercell. As a result, the screw dislocation is stabilized by its long-range elastic interactions with image dislocations in neighboring supercells, without the need for short-range pinning obstacles. However, one drawback of this setup is that the shear stress applied to the supercell has no resolved component on the original slip plane of the screw dislocation, such that the primary driving force for cross-slip is zero. As such, the calculated energy barriers are unrealistically high and the stress effects on energy barriers are too weak. These results are at variance with active cross-slip processes observed in experimental studies [34–36].

Another issue associated with the use of the NEB method for studying cross-slip in FCC metals is the need for reducing the length of the modeled portion along the MEP. We emphasize that the traditional NEB method [37] is inefficient, and often incapable, for capturing the saddle-point state of the stress-assisted, thermally-activated dislocation process in FCC metals. For such dislocation process, the saddle-point state often involves a collective displacement of a group of atoms along a dislocation line. As a result, the corresponding MEP is typically long and smooth. Since

the traditional NEB method requires the fixed initial and final states to be local minima in the potential energy landscape, a large number of nodes (i.e., replicas of the system) should be used to discretize the elastic band. This can ensure a sufficient nodal density for accurately mapping out the entire MEP, but is computationally inefficient because only a portion of the reaction path between the initial and saddle-point states is actually needed. The inefficiency issue is more significant when the MEP is distorted by a high load, such that the saddle-point state moves close to the initial state. In this case, finding the saddle-point state only requires the accurate mapping of a small portion of reaction path near the initial state. More importantly, when the final state is a local minimum, the corresponding dislocation core structure is usually very different from that at the saddle-point state. This large difference can cause a search for the most favorable saddle-point state to fail. To overcome these issues, we have previously developed the free-end NEB (FENEb) method [38,39] that can effectively reduce the path length of the modeled section along the MEP without sacrificing accuracy. This is realized by cutting short the elastic band and allowing the end of the shortened band to move freely on an energy iso-surface close to the initial state. This FENEb method allows an accurate determination of the saddle-point state at a much reduced computational cost [38–40]. It is noteworthy that Cai and co-workers have developed a different method that constrains the length of the modeled portion of the MEP and thus also enables an efficient search of the saddle-point state [25].

To study cross-slip by the FENEb method, it is critical to develop an effective procedure for generating a reasonable initial guess of the MEP. While it would be ideal to use MD simulations to achieve this goal, the timescale limitation and overdriven nature of MD often make it difficult to generate a cross-slip process with a local constriction between leading and trailing partial dislocations. To overcome this limitation, we used a facile procedure of locally-controlled shearing (LCS) [38,39] to generate a partial cross-slip along the screw dislocation line. Specifically, a relative shear displacement is imposed on a local region ahead of the leading partial, between two adjacent atomic layers on the cross-slip plane. This relative shear displacement is progressively increased to the partial Burgers vector length in several steps. At the end of each step, the selected region with imposed shear is held fixed, while the rest of the system is relaxed by the steepest descent or conjugate gradient method, so as to accommodate the imposed shear increment. This LCS procedure enables the controlled generation of partial cross-slip along the screw dislocation line at a specific location with a desired mode as discussed later.

In this work, we used the FENEb method [38,39], in conjunction with the LCS procedure, to determine the atomistic reaction pathways and energy barriers of cross-slip in a Ni single crystal. We focused on the cross-slip processes mediated by an array of pinning vacancy clusters in the form of stacking fault tetrahedra (SFTs). Parametric calculations were performed to study the effects of applied stress, obstacle spacing and size on the activation energy for cross-slip. We also studied a competing process of screw glide that involves the direct cutting of pinning SFTs on the original slip plane. Using FENEb-calculated energy barriers, we constructed dislocation mechanism maps to reveal the effects of resolved shear stress, obstacle spacing and size on the rate-controlling dislocation process. We further studied the activation volumes of cross-slip and obstacle-cutting. Our results for the latter process are consistent with the Nabarro scaling law for the linear dependence of activation volume on obstacle spacing [41], a relationship which has been used to support the well-known Cottrell-Stokes law of temperature-dependent work hardening [42]. The rest of this article is organized as follows. In Section 2, we describe the atomistic simulation setup and present several representative

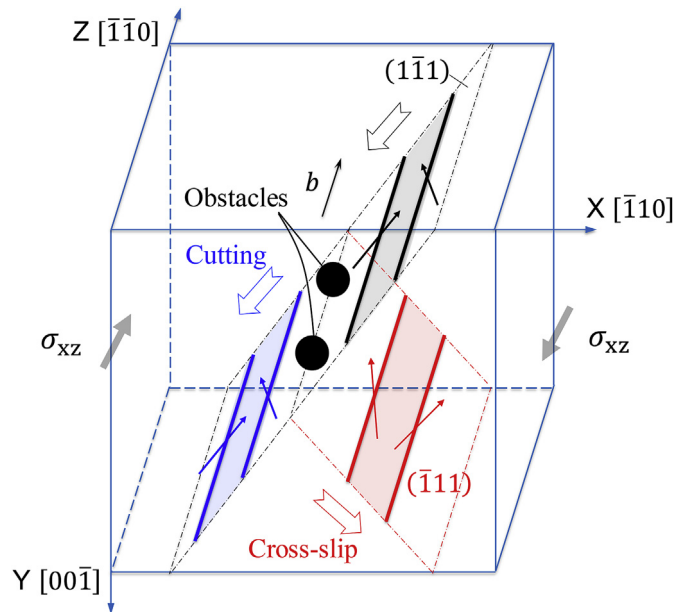


Fig. 1. Schematic illustration of cross-slip and obstacle-cutting by a screw dislocation. The simulation cell contains a screw dislocation in the $(\bar{1}\bar{1}1)$ slip plane. The screw dislocation is dissociated into the leading and trailing partials (black solid lines) with a stacking fault ribbon (gray area) in between. The Burgers vector $\vec{b} = \frac{1}{2}[\bar{1}\bar{1}0]$ is aligned with the Z direction. Two black dots represent obstacles that obstruct dislocation glide. Under an applied anti-plane shear stress σ_{xz} , the screw dislocation can either cross-slip onto the $(\bar{1}\bar{1}1)$ plane or cut through obstacles for continued glide on the $(\bar{1}\bar{1}1)$ plane.

FENEb results of cross-slip and obstacle-cutting. In Section 3, we examine the effects of obstacle spacing and size on cross-slip. Section 4 is devoted to the study of activation volumes of cross-slip and obstacle-cutting. These results are further discussed in Section 5.

2. Atomistic FENEb simulations

As schematically shown in Fig. 1, a screw dislocation in a simulation cell lies on the original slip plane of $(\bar{1}\bar{1}1)$ and is aligned along the $[\bar{1}\bar{1}0]$ direction, coinciding with the Z axis. Under an applied anti-plane shear stress σ_{xz} , the screw dislocation glides downward to the bottom surface of the simulation cell, but is obstructed by a periodic array of vacancy clusters. The breakaway of this screw dislocation from pinning obstacles can occur by either of the following two competing modes: (i) bypass of the pinning obstacles via cross-slip onto the $(\bar{1}\bar{1}1)$ plane, or (ii) direct cutting through the pinning obstacles for continued glide on the original slip plane. We performed atomistic simulations of screw cross-slip and obstacle-cutting using an in-house FENEb code [38] with an embedded atom method (EAM) potential of Ni [43,44]. All the atomic configurations presented are displayed using Atomeye [45].

2.1. Cross-slip

Fig. 2(a) shows the atomic configuration of the slab model in a supercell enclosed by a wireframe. The slab has the dimension of $9.9 \text{ nm} \times 16.1 \text{ nm} \times 11.9 \text{ nm}$ and contains a total of $\sim 153,000$ Ni atoms. Periodic boundary conditions are imposed in both the X- $[\bar{1}\bar{1}0]$ and Z- $[\bar{1}\bar{1}0]$ directions. The top and bottom surfaces of the slab, with the surface normal along the Y- $[001]$ direction, are traction free. A full screw dislocation is embedded in the center of the slab via the LCS procedure. It consists of a pair of leading and trailing partials, as shown in Fig. 2(b) and (c) with different visualization methods. A single vacancy cluster is embedded in the glide path of the screw dislocation in the supercell, and it represents an array of pinning obstacles along the dislocation line due to periodic boundary conditions applied, as schematically shown in Fig. 2(d). We applied the mechanical load by imposing an anti-plane shear strain to the supercell and then obtained the corresponding anti-plane shear stress σ_{xz} acting on the slab after energy minimization.

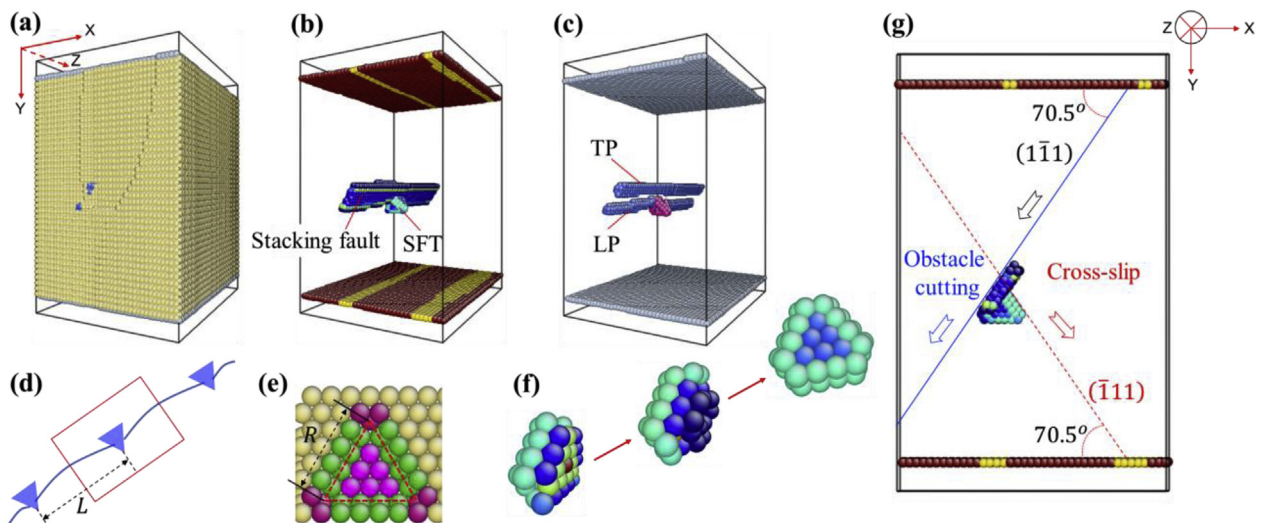


Fig. 2. Atomistic simulation setup and corresponding atomic configurations. (a) A slab of FCC Ni in a supercell, which contains a screw dislocation obstructed by a vacancy cluster. The X, Y and Z directions are identical to those shown in Fig. 1. Atoms are colored according to the coordination number N (yellow: $N = 12$; gray: $N = 8$; blue: $N = 13$). (b) Same as (a) except that atoms are colored according to the centrosymmetry parameter, thereby showing the stacking fault ribbon in between the leading and trailing partials of a screw dislocation. The vacancy cluster is in the form of the SFT. (c) Same as (a) except that atoms with the perfect coordination number ($N = 12$) are removed for clarity, thereby showing the core structures of the leading partial (LP) and trailing partial (TP). (d) Schematic of a screw dislocation line pinned by an array of SFTs with spacing L . The red box represents a supercell containing a single vacancy cluster, as shown in (a). (e) A triangle-shaped vacancy disk with size R ; atoms are colored according to the coordination number N . (f) Spontaneous transformation of an initial vacancy disk (left) into an SFT (right) during energy minimization; atoms are colored according to the centrosymmetry parameter. (g) Side view of the atomic configuration in (b); the obstructed screw dislocation can break away from the pinning SFT by either cross-slipping onto the $(\bar{1}\bar{1}1)$ slip plane and cutting through the SFT on the $(\bar{1}\bar{1}1)$ slip plane. (For interpretation of the references to color in this figure legend, the reader is referred to the Web version of this article.)

More specifically, Fig. 2(b) shows the relaxed atomic structure under an applied shear stress of $\sigma_{xz} = 109$ MPa. It is seen that the screw dislocation, which contains a stacking fault ribbon between the leading and trailing partial dislocations, is obstructed by a vacancy cluster in the supercell (corresponding to the cluster spacing $L \approx 12$ nm). In Fig. 2(c), the same atomic structure in Fig. 2(b) is colored according to the coordination number, so as to clearly display the leading and trailing partials. Fig. 2(e) and (f) show the spontaneous transformation of an initial disk-shaped vacancy cluster into an SFT during energy minimization. To create such a vacancy disk (Fig. 2(e)), we removed a small triangle patch of 15 atoms in a single atomic layer on the original slip plane of $(1\bar{1}1)$. As such, the vacancy disk has a nominal size R of 1.24 nm, corresponding to the five-atom side length of the triangle. During energy minimization, this vacancy disk spontaneously transforms into an SFT (Fig. 2(f)), as the void space of vacancies locally redistributes among the interstices of nearby atoms. Hereafter, the terms “vacancy cluster” and “SFT” are used interchangeably to refer to the same pinning obstacle. By considering the SFT as a stable obstacle with finite range and strength, we performed a parametric study of its effects on cross-slip and obstacle cutting. We note that the original slip plane of $(1\bar{1}1)$ and the cross-slip plane of $(\bar{1}11)$ have mirror symmetry with respect to the Y-Z plane, as shown in Fig. 2(g). As a result, the applied shear stress σ_{xz} renders an identical resolved shear stress on the two slip planes for driving the constriction and bow-out processes during cross-slip.

Our FENEB results reveal several competing modes of cross-slip, each of which corresponds to transfer of a screw dislocation from the original slip plane onto a different atomic layer of the cross-slip plane. The FENEB result in Fig. 3 shows a cross-slip mode that has a lower energy barrier than other modes and thus is energetically favorable at a low applied stress. In this case, the applied shear stress σ_{xz} is 109 MPa, giving a resolved shear stress τ of 94 MPa on the original slip plane of $(1\bar{1}1)$. Fig. 3(a) shows the converged MEP of cross-slip, when the free-end state has the same energy as the initial state. In all the MEPs presented in this work, the reaction coordinate is defined as the normalized path length along the MEP, and the energy of the initial state on the MEP is taken as zero. Fig. 3(b)–(i) show the dislocation structures along the MEP, and their corresponding energies are plotted as red circles in Fig. 3(a).

The dislocation structure in Fig. 3(b) is the initial state, corresponding to a local energy minimum on the MEP. The inset of Fig. 3(b) shows a schematic illustration of the leading and trailing partials of a screw dislocation interacting with an SFT. The leading partial is curved towards the SFT that acts as a trap of the screw dislocation. The curved part of the leading partial approaches a pure screw-like dislocation segment (highlighted by a short red line), which has a lower energy than other straight parts of the leading partial [17]. Cross-slip first initiates in this region, via a local constriction between the leading and trailing partials. Fig. 3(c) shows a subsequent bow-out process of the leading and trailing partials on the cross-slip plane of $(\bar{1}11)$. Due to SFT obstruction, the cross-slipped portion expands away from the SFT in a unidirectional manner (Fig. 3(d)). This behavior contrasts with the prediction of the Friedel-Escaig model, where the pinning obstacle is absent and hence the two constricted points move away from each other along the dislocation line in a bidirectional manner. At the saddle-point state (Fig. 3(e)), a part of the screw dislocation on the right side of the SFT has transferred onto the cross-slip plane, leaving the remaining part on the original slip plane. From the MEP in Fig. 3(a), the activation energy at the saddle point is determined as 1.03 eV. Beyond the saddle point, the cross-slipped part of the screw dislocation continues to expand (Fig. 3(f–h)), resulting in a continued energy decrease along the MEP (Fig. 3(a)). At the final state, the entire screw dislocation has cross-slipped onto the conjugate slip plane (Fig. 3(i)). The above cross-slip process along the MEP differs from the Friedel-Escaig model of cross-slip [6,7], principally in terms of the symmetry-breaking mode of unidirectional extension of cross-slip along the screw dislocation line, which is driven by SFT obstruction.

Fig. 4 shows a cross-slip mode that is energetically favorable at a high applied shear stress. In this mode, an applied shear stress σ_{xz} of 133 MPa results in a resolved shear stress τ of 115 MPa. We note that cross-slip in Fig. 4 occurs by transferring a screw dislocation from the original slip plane onto an atomic layer of the cross-slip plane that is different from that in Fig. 3. The MEP in Fig. 4(a) exhibits two energy barriers with one intermediate metastable state in between, which contrasts with a single energy barrier on the MEP shown in Fig. 3(a). The dislocation structures along the MEP are displayed in Fig. 4(b)–(g). The first saddle-point state (Fig. 4(c))

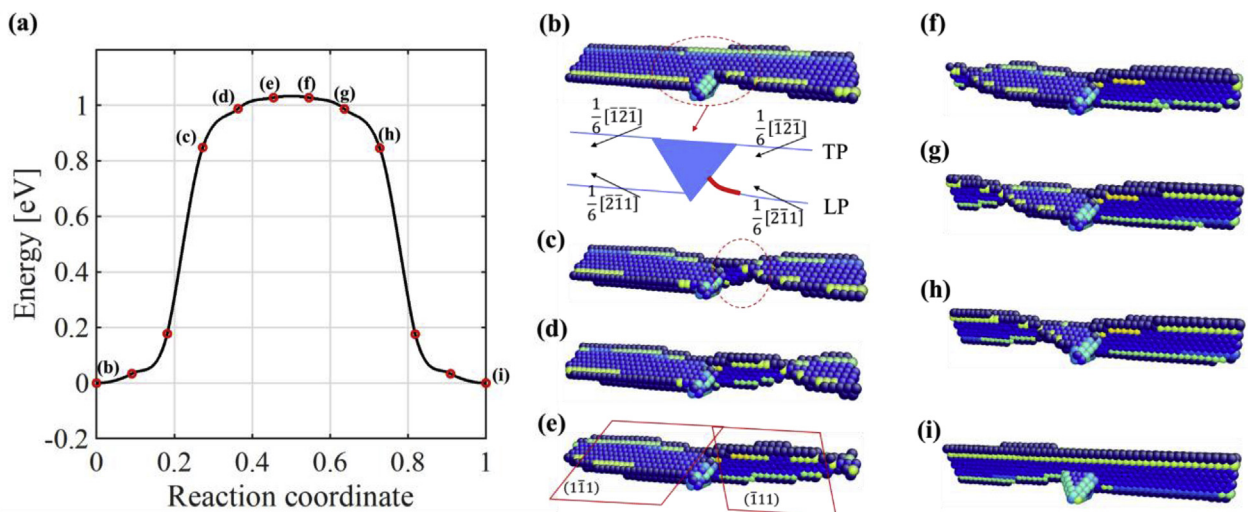


Fig. 3. FENEB result of the favorable cross-slip mode at a low resolved shear stress $\tau = 94$ MPa. A screw dislocation is obstructed by a vacancy cluster (i.e., SFT) in the supercell (corresponding to an array of obstacles with spacing $L = 12$ nm). (a) MEP of screw cross-slip when the free-end state is enforced to have the same energy as the initial state. (b)–(i) Atomic configurations of replicas along the MEP and their corresponding energies are plotted as red circles in (a). (For interpretation of the references to color in this figure legend, the reader is referred to the Web version of this article.)

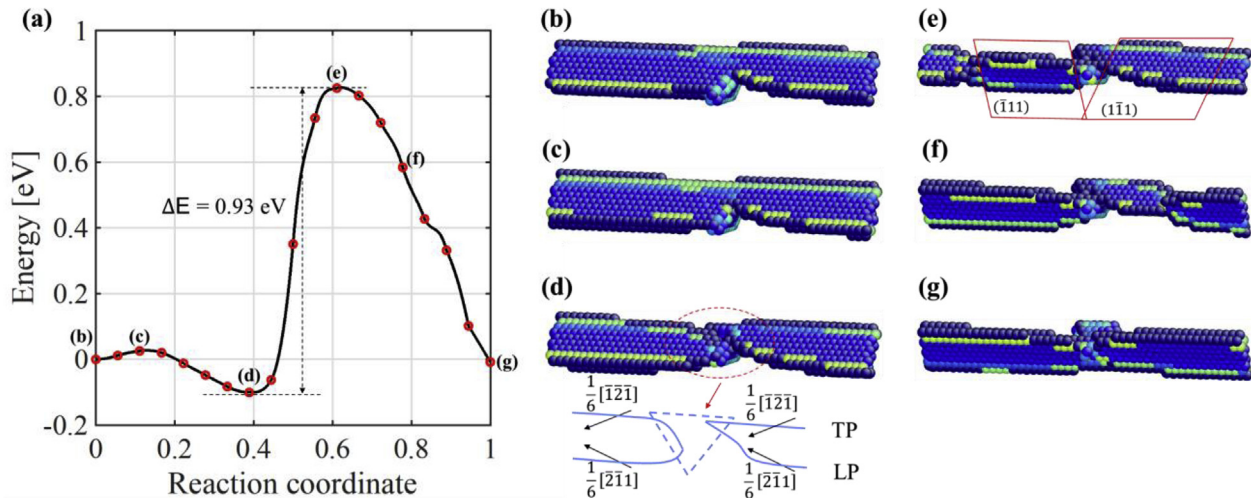


Fig. 4. FENEBC result of the most favorable mode of cross-slip at a high applied stress, i.e., resolved shear stress $\tau = 115$ MPa. The screw dislocation is obstructed by an SFT in the supercell (corresponding to an array of obstacles with a spacing of $L \approx 12$ nm). (a) MEP of screw cross-slip; the free-end state is enforced to have the same value as the initial state. (b–g) Atomic configurations of replicas along the MEP and their corresponding energies are plotted as red circles in (a). Note that the atomic configuration in (d) corresponds to a local energy minimum on the MEP in (a) and it has a lower energy than the initial state as shown in (b). (For interpretation of the references to color in this figure legend, the reader is referred to the Web version of this article.)

gives an energy barrier of 0.03 eV. The intermediate metastable state (Fig. 4(d)) corresponds to cutting of the SFT by the leading partial dislocation, as schematically illustrated in the inset of Fig. 4(d). The second saddle-point state gives a large energy barrier with a net value of 0.93 eV, when the energy of the metastable state (-0.1 eV) is taken as reference; this is the rate-limiting step of cross-slip along the MEP in Fig. 4(a). We note that the dislocation structure at the saddle-point state in Fig. 4(e) shows an initially cross-slipped segment on the left side of the SFT, which contrasts with an initially cross-slipped segment on the opposite side of the SFT in Fig. 3(e). Beyond the saddle point, the cross-slipped segment further grows in a unidirectional manner (Fig. 4(f)), resulting in a continued energy decrease along the MEP (Fig. 4(a)). At the final state (Fig. 4(g)), the entire screw dislocation has cross-slipped from the original slip plane of $(\bar{1}\bar{1}1)$ onto the conjugate slip plane of $(\bar{1}11)$.

2.2. Obstacle-cutting

We also performed FENEBC calculations to study obstacle-cutting by a screw dislocation on the original slip plane, which is an elementary process of plastic deformation that competes with cross-slip. While the cutting of SFTs by both edge and screw dislocations have been previously studied by MD simulations [46,47], we focus on the stress-dependent activation energies for this cutting process using FENEBC calculations. Fig. 5 shows the FENEBC results of obstacle-cutting under an applied shear stress σ_{xz} of 109 MPa, giving a resolved shear stress τ of 94 MPa on the original slip plane. The MEP in Fig. 5(a) exhibits two energy barriers and one intermediate local energy minimum in between. The initial state in Fig. 5(b) is identical to that in Fig. 3(b) with the same SFT size and spacing. However, in this case the FENEBC procedure enforces a requirement that the energy of the free-end state be lower than the

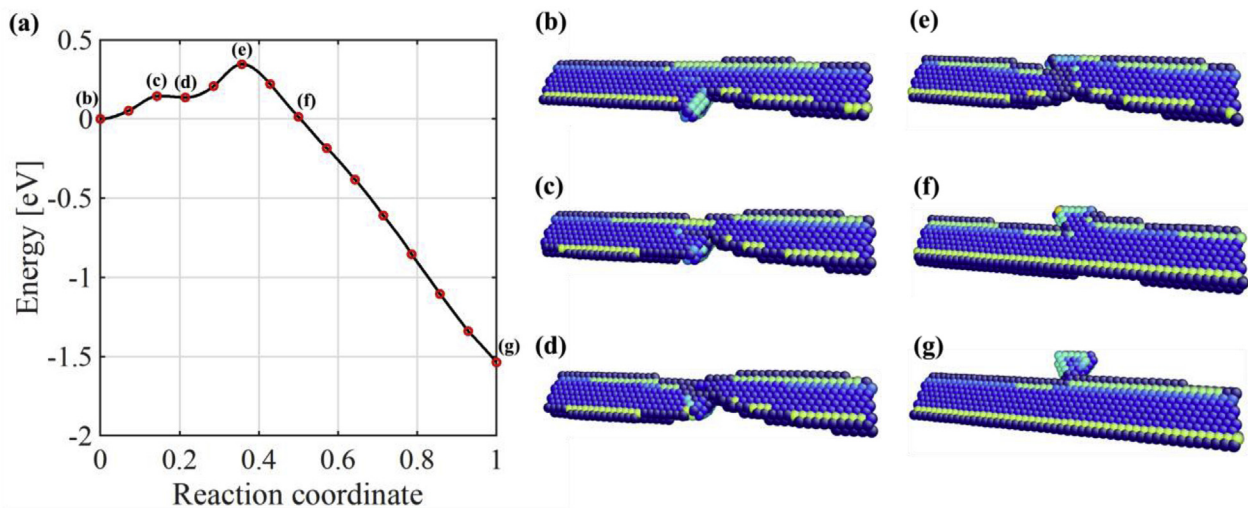


Fig. 5. FENEBC result for direct cutting of a pinning SFT. A screw dislocation is subjected to a resolved shear stress of $\tau = 94$ MPa and is obstructed by an SFT in the supercell (corresponding to an array of obstacles with a spacing of $L \approx 12$ nm). (a) MEP for SFT-cutting. (b)–(g) Atomic configurations of replicas along the MEP and their corresponding energies are plotted as red dots in (a). (For interpretation of the references to color in this figure legend, the reader is referred to the Web version of this article.)

initial state by 1.6 eV. As such, a sufficient separation is produced between the free-end state and the saddle-point state, which makes it easier to visualize the dislocation structure after obstacle-cutting. Fig. 5(c) shows the first saddle-point state of obstacle-cutting which is associated with trapping of the leading partial by the SFT, while Fig. 5(e) shows the second saddle-point state which involves depinning of the entire dislocation from the SFT. Similar to cross-slip, the dislocation structure during obstacle-cutting is asymmetric on the two sides of the SFT. The rate-limiting step of SFT-cutting is determined by the second saddle-point state, giving an energy barrier of 0.35 eV relative to the initial state. Beyond this saddle-point state, the screw dislocation breaks away from the SFT (Fig. 5(f) and (g)), resulting in a continued energy decrease along the MEP (Fig. 5(a)). Compared with the competing process of cross-slip under the same applied stress, SFT-cutting presents a lower energy barrier, making it the preferred deformation process.

To summarize, the above representative FENEBC results provide atomistically-detailed MEPs and energy barriers for cross-slip and obstacle-cutting by a screw dislocation pinned by an array of vacancy clusters, i.e., SFTs.

3. Effects of spacing and size of pinning obstacles

In this section, we focus on the FENEBC study of effects of stress, obstacle spacing and size on the energy barriers of cross-slip and cutting by a screw dislocation. In addition, various competing modes of cross-slip are further examined in detail. Using atomistically calculated energy barriers, we construct dislocation mechanism maps in the parameter space of resolved shear stress, obstacle spacing and size.

3.1. Obstacle spacing

To study the effects of obstacle spacing on cross-slip and cutting by a screw dislocation, we considered pinning SFTs with a fixed size R of 1.24 nm, as defined in Fig. 2(e). Compared to small obstacles such as a mono-vacancy or di-vacancy, these vacancy clusters in the form of SFTs are sufficiently large to trap the dislocation; however they are not over-sized, since larger vacancy clusters could lead to multiple reaction steps and energy barriers for dislocation-obstacle interactions, which would complicate the FENEBC calculation and analysis. Fig. 6(a) shows the activation energy for cross-slip as a function of resolved shear stress for different SFT spacings. In all the

cases, the activation energy decreases with increasing stress for a fixed SFT spacing, but a change of SFT spacing has a weak influence on the activation energy against stress curve. This trend will be further discussed in Section 4.1. Fig. 6(b) shows the activation energy for obstacle-cutting as a function of resolved shear stress for different SFT spacings. In all the cases, the activation energy decreases with increasing stress for a fixed SFT spacing. However, in contrast to cross-slip, the SFT spacing has a relatively strong influence on the activation energy against stress curve for obstacle-cutting. That is, at a given resolved shear stress, a smaller SFT spacing L leads to a higher activation energy. This arises because adjacent SFTs can impose an increasing pinning resistance with decreasing SFT spacing. Interestingly, the change of energy barrier with increased stress becomes more significant as the SFT spacing L becomes larger. In fact, the slope of the activation energy versus resolved shear stress curve is the so-called activation volume, which is an important parameter for characterizing the stress dependence of the activation energy. Fig. 6(b) indicates that the activation volume is quite sensitive to the SFT spacing L . Such a strong effect of SFT spacing on the activation energy for obstacle-cutting will be further discussed in Section 4.3, through a scaling analysis of activation volume with respect to obstacle spacing.

To understand the competition between cross-slip and obstacle-cutting, in Fig. 7(a) we compare their activation energies as a function of resolved shear stress for a fixed SFT spacing L of 6 nm. At low stresses, cross-slip exhibits lower activation energies than obstacle-cutting and thus is favored. With increasing stress, the two activation-energy curves cross at τ about 110 MPa, above which obstacle-cutting becomes favored. Based on the FENEBC-calculated activation energies of cross-slip and obstacle-cutting, we constructed a dislocation mechanism map Fig. 7(b), which shows the energetically favorable process in the parameter space of resolved shear stress and obstacle spacing. It is seen that cross-slip (indicated by red circles) predominates at low stresses and small SFT spacings, while obstacle-cutting (indicated by blue squares) predominates at high stresses and large SFT spacings.

3.2. Obstacle size

To study the effects of obstacle size on cross-slip and obstacle-cutting by a screw dislocation, we considered a fixed SFT spacing L of 12 nm. This spacing is more than six times that of the largest SFT size studied, such that the influence of SFT spacing can be

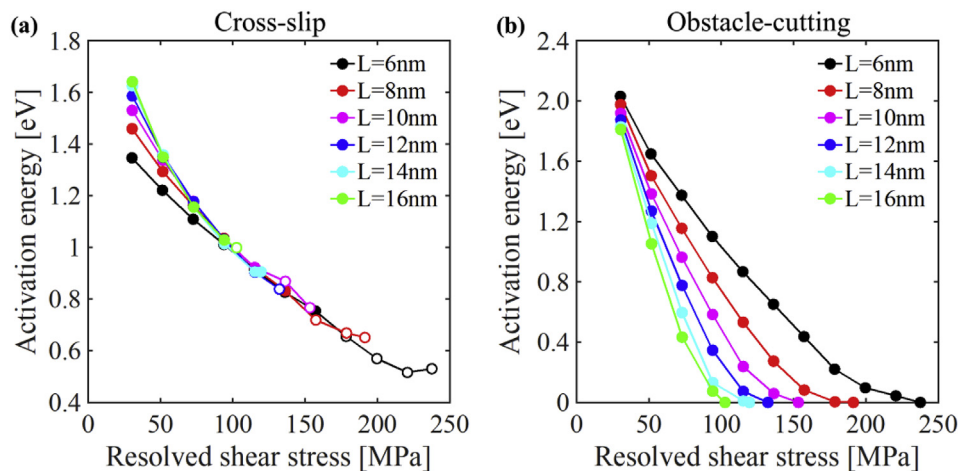


Fig. 6. Effects of SFT spacing L on the energy barriers of cross-slip and obstacle-cutting by a screw dislocation for a fixed SFT size $R = 1.24$ nm. (a) FENEBC results of the energy barrier of cross-slip versus resolved shear stress. (b) Same as (a) except for obstacle-cutting.

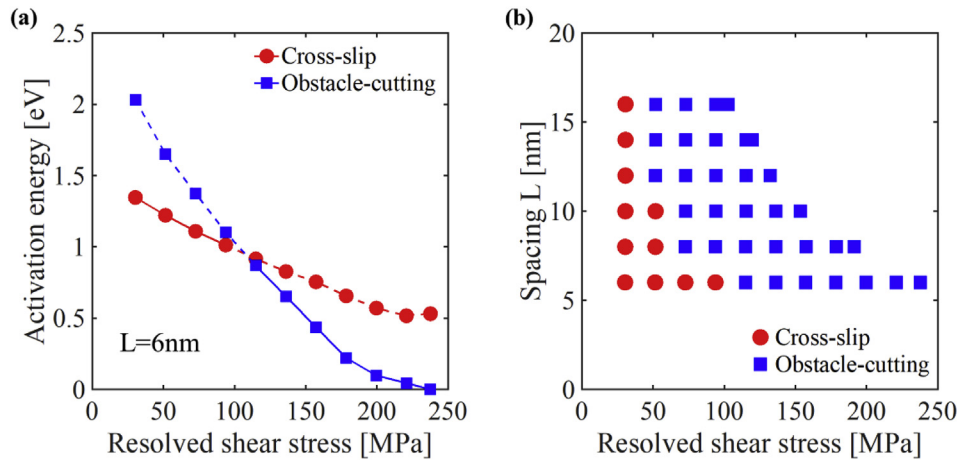


Fig. 7. Effects of SFT spacing on energy barriers of cross-slip and obstacle-cutting. (a) FENEBC results of activation energies of cross-slip and obstacle-cutting versus resolved shear stress for a fixed obstacle spacing, $L = 6$ nm. The solid line represents the energy barrier of the rate-controlling process. (b) Dislocation mechanism map in the parameter space of resolved shear stress and obstacle spacing, in which the energetically favored process with a relatively lower activation energy is marked.

clearly distinguished from that of SFT size. Fig. 8(a) shows the FENEBC-calculated activation energy of screw cross-slip as a function of resolved shear stress for different SFT sizes in the range of about 0.75–2 nm. For most SFT sizes studied (except for the smallest $R = 0.75$ nm), each activation-energy curve consists of two types of data points, i.e., the solid and hollow circles, which correspond to the cross-slip mode in Figs. 3 and 4, respectively. At a given resolved shear stress, the cross-slip mode with the lowest energy barrier is the rate-limiting cross-slip process, and its associated activation energy is plotted in Fig. 8(a) with the corresponding solid or hollow circle.

While the rate-limiting cross-slip processes in Fig. 8(a) involve two different modes, we actually have performed FENEBC calculations to study a total of six different cross-slip modes, as shown in Fig. 9 for the case of an SFT size R of 1.24 nm and an SFT spacing L of 12 nm. It is seen from Fig. 9(a) that the six cross-slip modes correspond to transfer of a screw dislocation from the original slip plane onto one of six atomic layers of the cross-slip plane, and each atomic layer is labeled by $n = 0, 1, 2, \dots, 5$, respectively. The previously described LCS procedure enabled the precise control of cross-slip onto a target atomic layer. The side view of the cross-slipped dislocation on each layer is shown in Fig. 9(b)–(g). At a given resolved shear stress, the cross-slip mode with the lowest energy

barrier is considered as the rate-limiting process. For example, Fig. 10 presents the FENEBC results for activation energy versus cross-slip layer n for different resolved shear stresses. To display the trend clearly, Fig. 10(a) and (b) show the activation energies at four low stresses and two high stresses, respectively; and the lowest cross-slip activation energies are marked by triangles. In Fig. 10(a), at a low applied stress, the activation energy of cross-slip onto the atomic layer $n = 0$ is the lowest (marked by a triangle) and is plotted as a pink solid circle in Fig. 8(a). The corresponding cross-slip mode along the MEP was shown earlier in Fig. 3. At a high applied stress, the activation energy of cross-slip onto atomic layer $n = 4$ is the lowest, as shown in Fig. 10(b). This same energy value is plotted as a pink hollow circle in Fig. 8(a). The corresponding cross-slip mode along the MEP was shown earlier in Fig. 4.

It is further seen from Fig. 8(a) that for large pinning SFTs ($R = 1.74$ nm and 1.99 nm), the activation energy does not change with the resolved shear stress monotonically. This trend arises due to change in the rate-limiting step of cross-slip, which involves the slip transfer onto a different atomic layer in the cross-slip plane, as discussed above. Moreover, even for a specific cross-slip mode with slip transfer onto the same atomic layer n , a larger resolved shear stress can give an unexpectedly higher activation energy, opposite to the usual trend of a decreasing activation energy with increasing

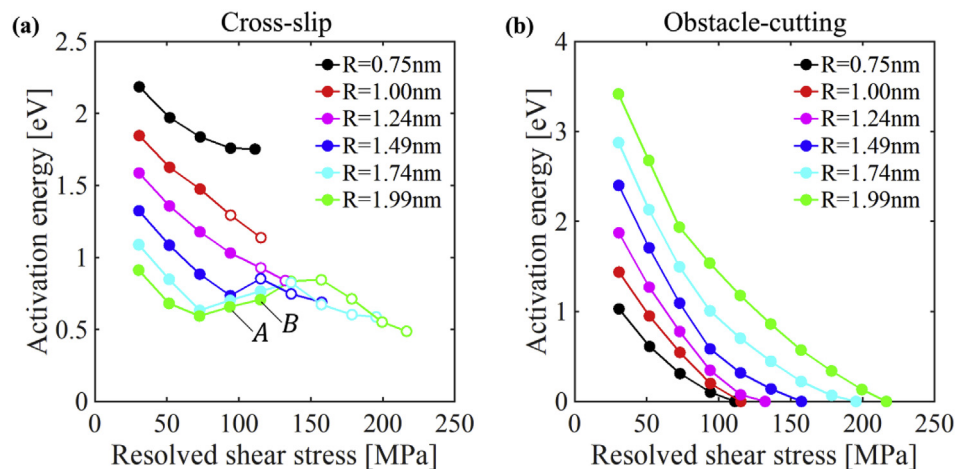


Fig. 8. Effects of SFT size R on the energy barriers of cross-slip and obstacle-cutting by a screw dislocation for a fixed obstacle spacing $L = 12$ nm. (a) FENEBC results of the energy barrier for cross-slip versus resolved shear stress. (b) Same as (a) except for obstacle-cutting.

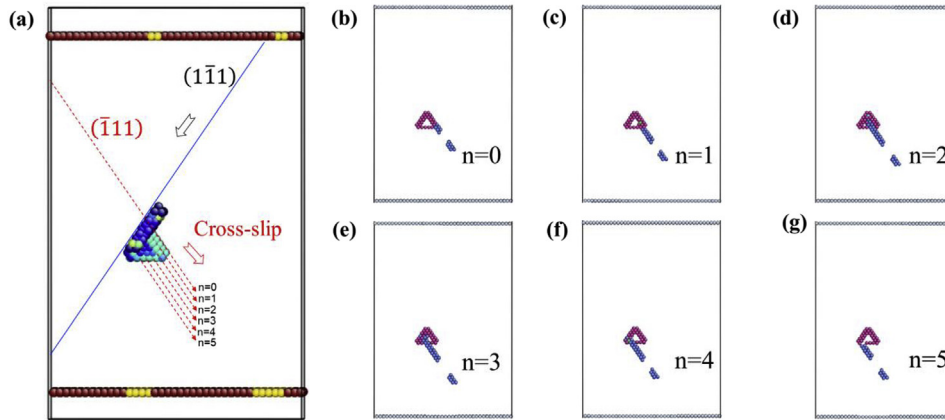


Fig. 9. Illustration of the six cross-slip modes studied. (a) A screw dislocation is transferred from the original slip plane onto one of the six atomic layers of the cross-slip plane, and each atomic layer is labeled by $n = 0, 1, 2, \dots, 5$. Atoms are colored according to the centrosymmetry parameter. (b)–(g) Cross-slipped dislocation in one of the six atomic layers of the cross-slip plane. Atoms are colored according to the coordinate number.

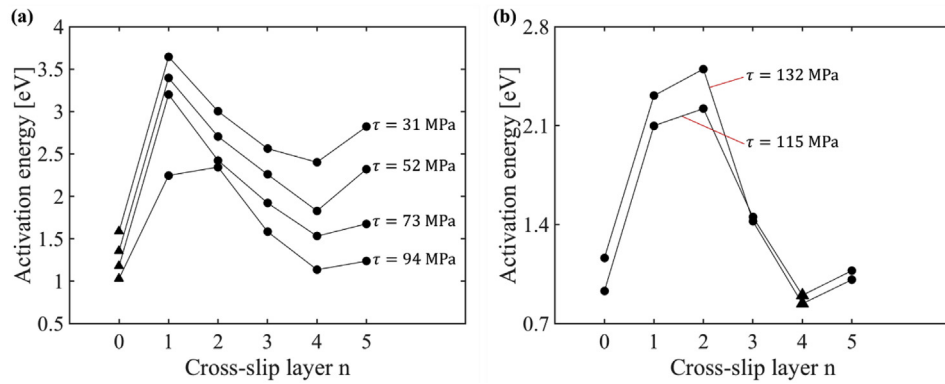


Fig. 10. Activation energy for screw cross-slip into one of the six atomic layers (labeled as n) of the cross-slip plane under (a) low and (b) high resolved shear stresses acting on the original slip plane.

stress. For example, in the case of $R = 1.99$ nm, as the resolved shear stress increases from $\tau = 94$ MPa to 115 MPa, the activation energy increases from 0.65 eV (marked as A) to 0.71 eV (marked as B) in Fig. 8(a). To understand this trend, we show in Fig. 11 the corresponding MEPs under the above two resolved shear stresses.

For each MEP, there are two saddle points, indicating two sequential steps in a cross-slip process. The first saddle point is associated with SFT-cutting by the leading partial and has a small energy barrier. The second saddle point (e.g., Fig. 11(c) or Fig. 11(e)) is associated with cross-slip and acts as the rate-controlling step. It

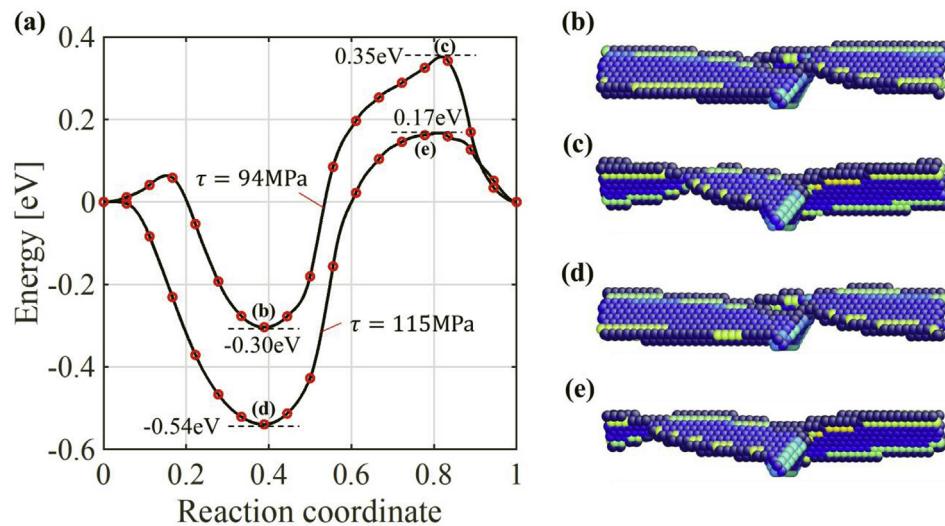


Fig. 11. Determination of the energy barrier of cross-slip when two saddle points are present on an MEP. (a) MEPs under the resolved shear stress $\tau = 94$ MPa and 115 MPa, respectively. (b)–(e) Dislocation structures along the two MEPs in (a).

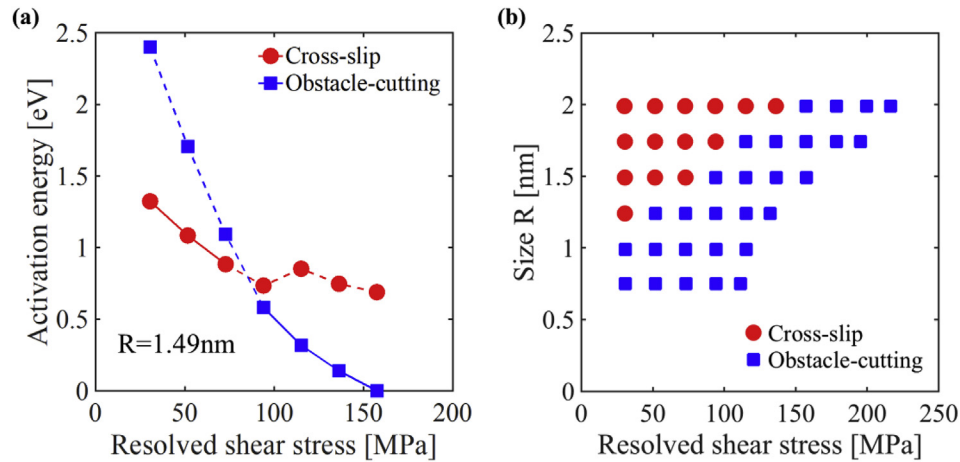


Fig. 12. Effects of obstacle size on energy barriers of cross-slip and obstacle-cutting. (a) FENEb results of activation energies of cross-slip and obstacle-cutting versus resolved shear stress for the fixed obstacle size $R = 1.49$ nm. The solid line represents the energy barrier of the rate-controlling process. (b) Dislocation mechanism map where the most favorable process with relatively low energy barrier is marked in the parameter space of resolved shear stress and obstacle size.

is noted that on each MEP, the energy of the local minimum state between the two saddle points is much lower than that of the initial state, and should be taken as the reference value for calculation of the activation energy of the second saddle point. Based on the energy values listed in Fig. 11(a), we obtained the cross-slip energy barrier of 0.65 eV under $\tau = 94$ MPa and 0.71 eV under $\tau = 115$ MPa. Hence, the increase in the energy barrier for cross-slip with stress can be primarily attributed to the decrease in the energy of the local minimum state between the two saddle points. This arises because the increasing stress promotes SFT-cutting during the first step, thus pushing forward the leading partial. As a result, cross-slip during the second step becomes difficult, since the leading partial must be pulled back from the SFT, so as to transfer onto the cross-slip plane.

To understand the effects of obstacle size on the competition between cross-slip and obstacle-cutting, in Fig. 12(a) we compare their energy barriers as a function of resolved shear stress for the fixed SFT size $R = 1.49$ nm and spacing $L = 12$ nm. At low stresses, cross-slip exhibits lower energy barriers than obstacle-cutting and thus is energetically favored. With increasing stress, the two energy-barrier curves cross over at $\tau \approx 100$ MPa, above which obstacle-cutting is energetically favored. Based on the FENEb-calculated energy barriers of cross-slip and obstacle-cutting, we constructed a dislocation mechanism map of the favored process in the parameter space of resolved shear stress and obstacle size, as shown in Fig. 12(b). It is seen that cross-slip predominates for low stresses and large obstacle sizes, while obstacle-cutting predominates for high stresses and small obstacle sizes. This result implies that large pinning vacancy clusters facilitate dislocation cross-slip. Related FENEb studies of size effects of other types of pinning obstacles, such as clusters of alloying elements, on dislocation cross-slip and cutting are in progress and will be reported in a subsequent paper.

4. Discussion

4.1. Effects of obstacles on cross-slip

Figs. 6 and 8 show the stress dependence of the activation energies for cross-slip and obstacle-cutting on SFT spacing and size. First, we notice that the SFT spacing L has a relatively weak influence on the activation energies for cross-slip, while the influence of the SFT size R is relatively strong. This observation can be

understood by considering interactions between the pinning SFT and screw dislocation. The dislocation structures along the MEP for cross-slip in Figs. 3 and 4 indicate that the pinning SFT has an attractive interaction with the screw dislocation, resulting in local trapping of the dislocation line into the SFT. It is known that the equilibrium distance d_0 between the leading and trailing partials (Fig. 13(a)) is controlled by the stacking fault energy and shear modulus [1]. Trapping of a dislocation line into the SFT can reduce the local separation between the leading and trailing partials to d_1 (Fig. 13(b)), thereby promoting cross-slip. However, the extent of the constriction can be presumably affected by the SFT pinning resistance and dislocation line tension. As seen in Fig. 3(b) and illustrated in Fig. 13(b), the trapping only affects a very small part of the dislocation line cutting into the SFT, which are indicative of the small pinning resistance of the SFT and/or the large line tension of the dislocation in the cases studied in this work. Such localized interaction between the SFT and dislocation line leads to a limited influence of SFT spacing on the activation energy for cross-slip. This conclusion is in accord with the FENEb result in Fig. 6(a), showing that the activation energy of cross-slip has a weak dependence on the SFT spacing. However, as shown in Fig. 8(a), the change of SFT size has a relatively large influence on the activation energy for cross-slip. The greater dependence on SFT size is due to the increased range of the local trapping interaction with the dislocation line when SFT sizes are increased.

We note that the EAM potential used in this work gives a low

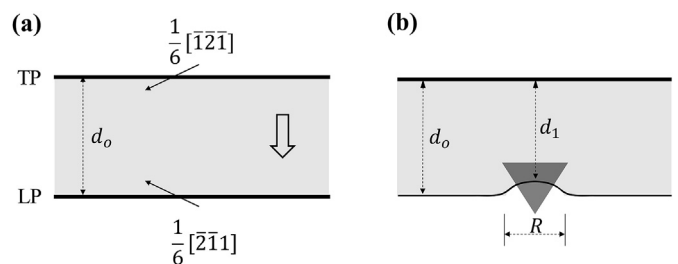


Fig. 13. Schematic illustration of interaction between screw dislocation and pinning obstacle. (a) When the pinning obstacle is absent, the screw dislocation dissociates into the straight leading partial (LP) and trailing partial (TP) with a stacking fault ribbon (gray area) of width d_0 in between. The arrow indicates the glide direction of the dislocation. (b) A pinning SFT of size R causes a local constriction between the LP and TP, such that the local spacing between the LP and TP is reduced to d_1 .

stacking fault energy of 89 mJ/m^2 relative to the corresponding experimental value of 125 mJ/m^2 [43]. As a result, the predicted equilibrium distance d_0 between the leading and trailing partials is relatively large and the activation energy of cross-slip is relatively high. This will affect the quantitative predictions of dislocation mechanism maps, such as the location of the boundary between the cross-slip and obstacle-cutting dominated regimes, but it is unlikely to change the qualitative feature of these maps. Song and Curtin [48] have developed a Ni-H potential that gives a more accurate stacking fault energy for Ni. It will be useful to compare the predictions of dislocation mechanism maps between the two Ni potentials in the future.

We also note that the present work is focused on the case when the glide plane of the incoming dislocation is the same as the base of the SFT. There is no obvious destruction/reconstruction of the SFT during cutting or cross-slip. Hence, we consider SFTs with different sizes and spacings as one class of stable obstacles that can effectively obstruct dislocation glide. However, there are possible cases where the incoming dislocation cuts through the SFT away from its base, as studied by previous molecular dynamics simulations [46,47]. In these cases, reconstruction of the SFT often occurs, leading to more complex reaction pathways of cutting and/or cross-slip. Their effects on dislocation mechanism maps warrant further study in the future.

4.2. Activation volume

The stress dependence of activation energy is usually characterized by the activation volume defined as

$$\Omega = -\frac{\partial E(\tau, R, L)}{\partial \tau} \quad (1)$$

where $E(\tau, R, L)$ denotes the activation energy that depends on the resolved shear stress τ on the original slip plane as well as the obstacle size R and spacing L . While the activation volume depends on stress in most cases, it is often treated as a constant when the range of stress change is not large. In Fig. 14, we show an example of determination of the activation volume for screw cross-slip and obstacle-cutting by taking numerical derivative for the $E(\tau, R,$

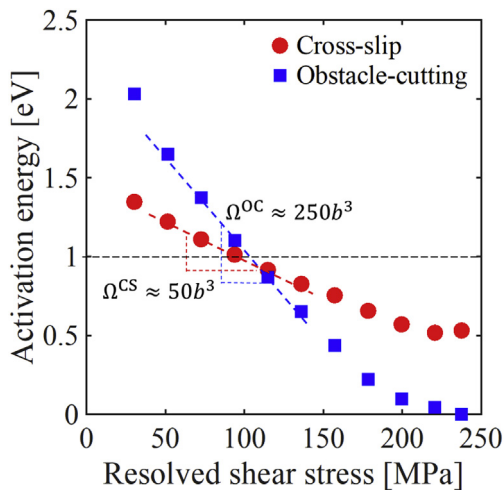


Fig. 14. Illustration of the activation volumes associated with cross-slip and obstacle-cutting by a screw dislocation, which can be determined from the slope of the respective curves of activation energy against resolved shear stress. The activation volumes of Ω^{CS} and Ω^{OC} for cross-slip (CS) and obstacle-cutting (OC) are determined at an activation energy level of 1 eV, for the case of SFT size $R = 1.24 \text{ nm}$ and spacing $L = 6 \text{ nm}$.

L) versus τ curve, as indicated by its slope, for the case of the SFT size $R = 1.24 \text{ nm}$ and spacing $L = 6 \text{ nm}$. According to transition state theory, to achieve a reasonable frequency (e.g., 1/s) of screw cross-slip or obstacle-cutting relevant to laboratory experiments, the energy barrier should be on the order of $30 k_B T$ (where k_B is Boltzmann's constant and T is the absolute temperature) [49], which is about 0.75 eV at room temperature. Hence, we considered the activation volume at a representative activation energy value of 1 eV and calculated the activation volume for cross-slip as $\Omega^{\text{CS}} \approx 50b^3$ (where b is the Burgers vector length of a full dislocation in Ni), which is much smaller than that of obstacle-cutting $\Omega^{\text{OC}} \approx 250b^3$. The different activation volumes for cross-slip and obstacle-cutting clearly reflect the different rates of change of activation energy with respect to resolved shear stress around the activation energy of 1 eV, as seen from Fig. 14.

4.3. Nabarro's scaling law for activation volume

An important effect of obstacle spacing on the activation energy for obstacle-cutting is revealed in Fig. 6(b), which shows that the change of activation energy for obstacle-cutting with resolved shear stress becomes more significant as the obstacle spacing L becomes larger. Using the concept of activation volume discussed in Section 4.2, one can interpret the results in Fig. 6(b) in terms of increasing activation volume (i.e., the slope of energy barrier curves) with obstacle spacing L .

Nabarro [41] has derived a scaling law between activation volume Ω and obstacle spacing L by considering the thermal activation of dislocation bow-out between obstacles, i.e.,

$$\Omega \propto Lb^2 \quad (2)$$

He emphasized that the scaling law in Eq. (2) holds if the obstacles are of finite strength and range instead of infinite strength. Obstacles such as atomically-sized vacancy clusters and alloying clusters usually have finite strength and range, such that the dislocation line can cut through them. Only in cases where the obstacle effectively has an infinitely large strength would the dislocation line loop around the obstacle without cutting through it; in these cases, the scaling relation would be different from Eq. (2) and given by $\Omega \propto L^2b$. Nabarro used the scaling law in Eq. (2) to rationalize the well-known Cottrell-Stokes law for temperature-dependent strain hardening in FCC metals [42]. To this end, he considered an analogue of the Cottrell-Stokes Law in which changes of temperature at a given strain rate are replaced by their inverse, changes of strain rate at a given temperature. Nabarro further showed that since the critical resolved stress τ for cutting through pinning obstacles scales as

$$\tau \propto \mu b/L \quad (3)$$

where μ denotes the shear modulus, the product of τ and Ω (based on Eqs. (2) and (3)) should remain a constant independent of the obstacle spacing L .

To validate Nabarro's scaling law using the present FENE results, we show in Fig. 15(a) the representative activation energy curves of cutting for two different obstacle spacings. At the same value of activation energy (e.g. 1 eV, indicated by the dashed line), one can calculate the activation volume Ω_i^{OC} from the two curves and record the corresponding resolved shear stress τ_i . According to Nabarro's scaling law, the calculated products of τ_i and Ω_i^{OC} should be the same for both curves. To validate this idea, we first fit the activation energy curves in Fig. 6(b) using a nonlinear function $E(\tau) = A(1 - \tau/\tau_a)^\alpha$, where A , τ_a and α are the fitting parameters, and then calculated the activation volume according to Eq. (1). At

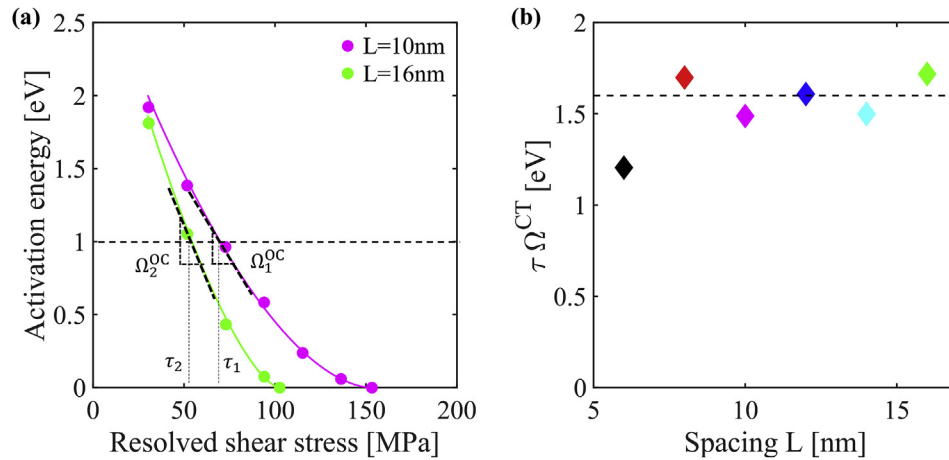


Fig. 15. Validation of the Nabarro scaling law between activation volume and obstacle spacing, based on the FENEb results of obstacle-cutting (OC). (a) Evaluation of activation volumes Ω_i^{OC} and critical resolved shear stress τ_i at the activation energy of 1 eV for two obstacle spacings, $L = 10$ nm and 16 nm. (b) The product of τ_i and Ω_i^{OC} is approximately a constant (indicated by the dashed line) for different obstacle spacings.

an activation energy value of 1 eV, we calculated the products of τ_i and Ω_i^{OC} for different obstacle spacings. As shown in Fig. 15(b), the products of τ_i and Ω_i^{OC} remain around 1.6 eV, except for the case of a very small obstacle spacing that arises due to a strong nonlinear effect of obstacle spacing on the activation volume and/or critical shear stress. Hence, the present atomistic FENEb results for obstacle-cutting directly validate Nabarro's scaling law for cases with small obstacle spacings between 5 and 10 nm. This result emphasizes the practical importance of accounting for finite strengths of pinning obstacles, such as vacancy clusters. It also reinforces the notion that the finite strength is an obstacle attribute that underlies the Cottrell-Stokes law of temperature-dependent strain hardening in FCC metals.

Finally, we note that from Fig. 8(b), the activation volumes for cross-slip mediated by vacancy clusters (i.e., slopes of curves in Fig. 8(b)) appear to depend only weakly on obstacle spacing. This weak dependence is likely due to the short-range nature of the interactions between pinning clusters and the dislocation line (as discussed in Section 4.1). Hence, due to the limited range of obstacle spacings studied by the present FENEb calculations, cross-slip mediated by vacancy clusters cannot be used to compare with Nabarro's scaling law.

5. Conclusions

We have performed FENEb calculations to determine the activation energy for cross-slip of a screw dislocation obstructed by an array of vacancy clusters in the form of SFTs. We have also studied a competing process of direct cutting of pinning SFTs by the screw dislocation for continued glide on the original slip plane. The activation energies of both cross-slip and obstacle-cutting are determined for different applied shear stresses, obstacle spacings and sizes. These atomistically-determined energy barriers enable us to construct dislocation mechanism maps for revealing the effects of resolved shear stress, obstacle size and spacing on the rate-controlling dislocation process. In addition, our FENEb results show that the activation volume of obstacle-cutting mediated by SFTs scales linearly with obstacle spacing. This result is consistent with Nabarro's scaling law of Eq. (2) and thereby emphasizes the importance of the finite strengths of pinning obstacles, such as vacancy clusters.

Cottrell analyzed the temperature-dependent flow stress of FCC metals between near-zero and room temperature, and emphasized

that “the observed temperature dependence of the flow stress indicates, importantly, that major obstacles contributing to work hardening are highly localized, on an atomic scale.” [50] Our work demonstrates the effectiveness of FENEb calculations for investigating effects of atomically-sized obstacles, e.g., pinning vacancy clusters, on stress-assisted, thermally-activated dislocation processes such as cross-slip and obstacle-cutting. FENEb studies on other types of atomically-sized obstacles such as interstitial hydrogen atoms or substitutional alloying atoms and their clusters are in progress. These additional FENEb results, along with this work, are directed at shedding light on the controlling deformation mechanisms in FCC metals and alloys, which may advance the fundamental understanding of hydrogen embrittlement in stainless steels, of strengthening effects of concentrated solute clusters on dislocations in high-entropy alloys, and of other related phenomena of scientific and technological interest.

References

- [1] D. Hull, D.J. Bacon, *Introduction to Dislocations*, Elsevier, 2011.
- [2] J.J. Gilman, *Micromechanics of Flow in Solids*, McGraw-Hill, New York, NY, 1969.
- [3] A.S. Argon, *Strengthening Mechanisms in Crystal Plasticity*, Oxford University Press Inc., New York, 2008.
- [4] U. Essmann, H. Mughrabi, Annihilation of dislocations during tensile and cyclic deformation and limits of dislocation densities, *Philos. Mag. A* 40 (1979) 731–756.
- [5] R. Fleischer, Cross slip of extended dislocations, *Acta Metall.* 7 (1959) 134–135.
- [6] G.M. Friedel J, in: Rassweiler, W.L. Grube. *Internal Stresses and Fatigue in Metals: Proceedings*, Elsevier Pub. Co., 1959.
- [7] B. Escaig, L'activation thermique des déviations sous faibles contraintes dans les structures hc et cc Par, *Phys. Status Solidi* 28 (1968) 463–474.
- [8] A. Stroh, Constrictions and jogs in extended dislocations, *Proc. Phys. Soc. B* 67 (1954) 427.
- [9] H. Wolf, Die Aktivierungsenergie für die Quergleitung aufgespaltener Schraubenversetzungen, *Z. Naturforsch.* 15 (1960) 180–193.
- [10] W. Püschl, The energy of constrictions in extended dislocations, *Phys. Status Solidi* 162 (1990) 363–370.
- [11] G. Saada, Cross-slip and work hardening of fcc crystals, *Mater. Sci. Eng.* 137 (1991) 177–183.
- [12] W. Püschl, G. Schoeck, Calculation of cross-slip parameters in fcc crystals, *Mater. Sci. Eng.* 164 (1993) 286–289.
- [13] W. Püschl, Models for dislocation cross-slip in close-packed crystal structures: a critical review, *Prog. Mater. Sci.* 47 (2002) 415–461.
- [14] J. Gagel, D. Weygand, P. Gumbsch, Formation of extended prismatic dislocation structures under indentation, *Acta Mater.* 111 (2016) 399–406.
- [15] E. Bitzek, C. Brandl, P. Derlet, H. Van Swygenhoven, Dislocation cross-slip in nanocrystalline fcc metals, *Phys. Rev. Lett.* 100 (2008) 235501.
- [16] T. Rasmussen, K.W. Jacobsen, T. Leffers, O.B. Pedersen, S. Srinivasan, H. Jonsson, Atomistic determination of cross-slip pathway and energetics,

- Phys. Rev. Lett. 79 (1997) 3676.
- [17] T. Rasmussen, K.W. Jacobsen, T. Leffers, O.B. Pedersen, Simulations of the atomic structure, energetics, and cross slip of screw dislocations in copper, *Phys. Rev. B* 56 (1997) 2977.
- [18] M. Wen, S. Fukuyama, K. Yokogawa, Hydrogen-affected cross-slip process in fcc nickel, *Phys. Rev. B* 69 (2004) 174108.
- [19] M. Wen, S. Fukuyama, K. Yokogawa, Cross-slip process in fcc nickel with hydrogen in a stacking fault: an atomistic study using the embedded-atom method, *Phys. Rev. B* 75 (2007) 144110.
- [20] T. Hatano, T. Kaneko, Y. Abe, H. Matsui, Void-induced cross slip of screw dislocations in fcc copper, *Phys. Rev. B* 77 (2008), 064108.
- [21] S. Rao, D. Dimiduk, J. El-Awady, T. Parthasarathy, M. Uchic, C. Woodward, Activated states for cross-slip at screw dislocation intersections in face-centered cubic nickel and copper via atomistic simulation, *Acta Mater.* 58 (2010) 5547–5557.
- [22] S. Rao, D. Dimiduk, T. Parthasarathy, J. El-Awady, C. Woodward, M. Uchic, Calculations of intersection cross-slip activation energies in fcc metals using nudged elastic band method, *Acta Mater.* 59 (2011) 7135–7144.
- [23] S. Rao, D. Dimiduk, T. Parthasarathy, M. Uchic, C. Woodward, Atomistic simulations of surface cross-slip nucleation in face-centered cubic nickel and copper, *Acta Mater.* 61 (2013) 2500–2508.
- [24] S. Rao, D. Dimiduk, J. El-Awady, T. Parthasarathy, M. Uchic, C. Woodward, Screw dislocation cross slip at cross-slip plane jogs and screw dipole annihilation in FCC Cu and Ni investigated via atomistic simulations, *Acta Mater.* 101 (2015) 10–15.
- [25] K. Kang, J. Yin, W. Cai, Stress dependence of cross slip energy barrier for face-centered cubic nickel, *J. Mech. Phys. Solid.* 62 (2014) 181–193.
- [26] S. Xu, L. Xiong, Y. Chen, D.L. McDowell, Shear stress-and line length-dependent screw dislocation cross-slip in FCC Ni, *Acta Mater.* 122 (2017) 412–419.
- [27] W.G. Nöhring, W. Curtin, Dislocation cross-slip in fcc solid solution alloys, *Acta Mater.* 128 (2017) 135–148.
- [28] H. Jonsson, G. Mills, K.W. Jacobsen, Nudged elastic band method for finding minimum energy paths of transitions, in: B.J. Berne, G. Ciccotti, D.F. Coker (Eds.), *Classical and Quantum Dynamics in Condensed Phase Simulations*, 1998, pp. 385–404.
- [29] T. Zhu, J. Li, S. Yip, Atomistic reaction pathway sampling: the nudged elastic band method and nanomechanics applications, in: H.D. Espinosa, G. Bao (Eds.), *Nano and Cell Mechanics*, John Wiley & Sons, 2013, pp. 313–338.
- [30] J.H. Weiner, *Statistical Mechanics of Elasticity*, Dover, New York, 2002.
- [31] T. Zhu, J. Li, Ultra-strength materials, *Prog. Mater. Sci.* 55 (2010) 710–757.
- [32] T. Zhu, J. Li, S. Ogata, S. Yip, Mechanics of ultra-strength materials, *MRS Bull.* 34 (2009) 167–172.
- [33] C. Jin, Y. Xiang, G. Lu, Dislocation cross-slip mechanisms in aluminum, *Phil. Mag.* 91 (2011) 4109–4125.
- [34] J. Bonneville, B. Escaig, Cross-slipping process and the stress-orientation dependence in pure copper, *Acta Metall.* 27 (1979) 1477–1486.
- [35] J. Bonneville, B. Escaig, J. Martin, A study of cross-slip activation parameters in pure copper, *Acta Metall.* 36 (1988) 1989–2002.
- [36] J. Kacher, G. Liu, I. Robertson, In situ and tomographic observations of defect free channel formation in ion irradiated stainless steels, *Micron* 43 (2012) 1099–1107.
- [37] G. Henkelman, G. Johansson, H. Jonsson, Methods for finding saddle points and minimum energy paths, in: S.D. Schwartz (Ed.), *Progress on Theoretical Chemistry and Physics*, Kluwer Academic, 2000, pp. 269–300.
- [38] T. Zhu, J. Li, A. Samanta, H.G. Kim, S. Suresh, Interfacial plasticity governs strain rate sensitivity and ductility in nanostructured metals, *Proc. Natl. Acad. Sci. Unit. States Am.* 104 (2007) 3031–3036.
- [39] T. Zhu, J. Li, A. Samanta, A. Leach, K. Gall, Temperature and strain-rate dependence of surface dislocation nucleation, *Phys. Rev. Lett.* 100 (2008), 025502.
- [40] Q.-J. Li, B. Xu, S. Hara, J. Li, E. Ma, Sample-size-dependent surface dislocation nucleation in nanoscale crystals, *Acta Mater.* 145 (2018) 19–29.
- [41] F. Nabarro, Cottrell-Stokes law and activation theory, *Acta Metall. Mater.* 38 (1990) 161–164.
- [42] A.H. Cottrell, R.J. Stokes, Effect of temperature on the plastic properties of aluminium crystals, *Proceedings of the Royal Society A* 233 (1955) 17–34.
- [43] J.E. Angelo, N.R. Moody, M.I. Baskes, Trapping of hydrogen to lattice defects in nickel, *Model. Simulat. Mater. Sci. Eng.* 3 (1995) 289.
- [44] M. Baskes, X. Sha, J. Angelo, N. Moody, Trapping of hydrogen to lattice defects in nickel, *Model. Simulat. Mater. Sci. Eng.* 5 (1997) 651.
- [45] J. Li, AtomEye: an efficient atomistic configuration viewer, *Model. Simulat. Mater. Sci. Eng.* 11 (2003) 173–177.
- [46] D. Bacon, Y. Osetsky, D. Rodney, Dislocation–obstacle interactions at the atomic level, *Dislocations in Solids* 15 (2009) 1–90.
- [47] B. Wirth, V. Bulatov, T.D. de la Rubia, Dislocation–stacking fault tetrahedron interactions in Cu, *J. Eng. Mater. Technol.* 124 (2002) 329–334.
- [48] J. Song, W. Curtin, A nanoscale mechanism of hydrogen embrittlement in metals, *Acta Mater.* 59 (2011) 1557–1569.
- [49] A.H. Cottrell, Thermally activated plastic glide, *Phil. Mag. Lett.* 82 (2002) 65–70.
- [50] A.H. Cottrell, A brief view of work hardening, in: F.R.N. Nabarro, M.S. Duesbery (Eds.), *Dislocations in Solids*, Elsevier, Amsterdam, 2002, pp. vii–xvii.